New Journal of Physics
The open access journal at the forefront of physics

Deutsche Physikalische Gesellschaft DPG IOP Institute of Physics

PAPER • OPEN ACCESS

Pattern formation on Ge by low energy ion beam erosion

To cite this article: Marc Teichmann *et al* 2013 *New J. Phys.* **15** 103029

New Journal of Physics
The open access journal for physics

Pattern formation on Ge by low energy ion beam erosion

Marc Teichmann[1,3], Jan Lorbeer[1], Bashkim Ziberi[2], Frank Frost[1] and Bernd Rauschenbach[1]

[1] Leibniz-Institut für Oberflächenmodifizierung (IOM), Permoserstrasse 15, D-04318 Leipzig, Germany
[2] Faculty of Natural Sciences and Mathematics, State University of Tetova, Bul. Ilinden bb, 1200 Tetova, Macedonia
E-mail: marc.teichmann@iom-leipzig.de

New Journal of Physics **15** (2013) 103029 (25pp)
Received 10 July 2013
Published 28 October 2013
Online at http://www.njp.org/
doi:10.1088/1367-2630/15/10/103029

Abstract. Modification of nanoscale surface topography is inherent to low-energy ion beam erosion processes and is one of the most important fields of nanotechnology. In this report a comprehensive study of surface smoothing and self-organized pattern formation on Ge(100) by using different noble gases ion beam erosion is presented. The investigations focus on low ion energies ($\leqslant 2000$ eV) and include the entire range of ion incidence angles. It is found that for ions (Ne, Ar) with masses lower than the mass of the Ge target atoms, no pattern formation occurs and surface smoothing is observed for all angles of ion incidence. In contrast, for erosion with higher mass ions (Kr, Xe), ripple formation starts at incidence angles of about 65° depending on ion energy. At smaller incident angles surface smoothing occurs again. Investigations of the surface dynamics for specific ion incidence angles by changing the ion fluence over two orders of magnitude gives a clear evidence for coarsening and faceting of the surface pattern. Both observations indicate that gradient-dependent sputtering and reflection of primary ions play crucial role in the pattern evolution, just at the lowest accessible fluences. The results are discussed

[3] Author to whom any correspondence should be addressed.

in relation to recently proposed redistributive or stress-induced models for pattern formation. In addition, it is argued that a large angular variation of the sputter yield and reflected primary ions can significantly contribute to pattern formation and evolution as nonlinear and non-local processes as supported by simulation of sputtering and ion reflection.

Contents

1. Introduction

For particular sputtering conditions with low- and medium-energy ions self-organized nanostructures can evolve on solid surfaces. In the last decades, a large variety of evolving surface structures are observed, such as periodic ripple patterns and arrays of dots or holes. These pattern formations are also found on many different materials, for instance metals [1–7], semiconductors [8–15] as well as various compounds [16–20]. Special attention is focused on Si as an important material for technical applications. Additionally, it is a simple one-component system and readily amorphizes during ion irradiation that makes it a feasible model system for revealing the processes behind patterning and smoothing. Many investigations on the pattern formation process have been recently done for Si [21–25]. It has been found that, at low incident angles the surface remains flat up to a critical angle when ripple formation starts. This angle slightly depends on ion energy as well as on the ion species. Additionally, observations suggested that the metal incorporation during ion sputtering also plays an important role in the pattern formation. Dots and ripple formation takes place under near-normal incidence with simultaneous metal deposition whereas the surface remains flat without metal incorporation [25–32]. The first model that describes the ripple formation process is the erosion-based theory of Bradley and Harper (BH) [33], which combines surface-curvature-dependent sputtering for surface destabilization with a temperature-dependent surface diffusion which tends to smooth the surface. However, this model cannot explain a number of experimental observations, such as smoothing of the surface for small angles of incidence and a transition from smooth to rippled surfaces with increasing ion incidence angle as observed for Si or Ge.

A modification of this model has been proposed by Carter and Vishnyakov (CV) [34], which is able to overcome this discrepancy for small angles of incidence. The CV model comprises a curvature-dependent ballistic drift due to momentum transfer during ion bombardment as smoothing mechanism, which can be regarded as an effective downhill current of surface atom counteracting the BH instability. In consequence, the ripple evolution cannot occur if ballistic drift can compensate curvature-dependent sputtering. The model explains the smoothening for normal and near-normal incidence and predicts a critical angle as the starting point for roughening. A further development of this model was done by Madi *et al* [35]. In their approach, the curvature coefficients from the linear analysis of a surface height profile are decomposed into an erosive (BH) and an ion-stimulated mass redistribution (CV) component. Both parts are modified with the empirical Yamamura correction factor. Hence, the model gets along with one adjustable parameter and it is able to explain the experimental results for Ar irradiation of Si. At a microscopic scale, significant new insights are gained from molecular dynamics (MD) simulations. Thus, Moseler *et al* [36] have been shown that an impact-induced downhill current is important for smoothening of amorphous materials. In a more general methodology, Norris *et al* [37, 38] made MD simulations of craters caused by individual ion impacts. The ion -incidence-angle-dependent moments of the crater function are calculated and upscaled to a continuum partial differential equation. The calculated moments consist again of an erosive and redistributive part. The analysis of surface stability has been done based on curvature coefficients that have been obtained from the first moments of the crater function. It has been shown that the redistributive part can prevail against erosive effects and it determines the pattern formation [38]. Sample calculations were made for Ar irradiation on Si for two energies (100 and 250 eV), which show a good agreement with experimental results [23]. More recently, stress-induced solid flow models are developed [39–41]. In these models, the rearrangement of surface atoms is driven by the stress caused by ion irradiation of a thin surface layer. A detailed analysis of these models reveals again an accurate description of the scenario observed for Ar ion erosion of Si at rather low ion energies [40, 41].

Particularly in view of these different models, experimental studies of (supposedly) simple ion/target combination are indispensable to validate the various approaches. Therefore, in order to substantiate present models and to close the lack in experimental results, low-energy ion beam erosion of Ge is investigated. Similar to Si, Ge is an important material for technical applications and is also a simple one-component system which makes it easier to reveal the key processes in pattern formation. In addition, it is an amorphizable monoelemental target and the direct counterpart to Si, except for the higher mass of target atoms. For ion beam erosion of Ge, there are only a few reports concerning this topic up to now [42–47]. In the first study, ion erosion with 1 keV Xe ions at 55° results in ripple formation, if the surface remains crystalline during bombardment (for temperatures $> 150\,^{\circ}$C). In contrast, surface smoothing occurs at room temperature, where the surface becomes amorphisized. The first more comprehensive study on this topic was done by Ziberi *et al* [45] but they might deal with metallic contaminations in their setup which can contribute to a different behavior in pattern formation process as it has been shown for Si [31]. The same behavior is probably also true for the dot and ripple pattern reported for 1 keV Xe ion bombardment at near-normal incidence [44]. For low-contamination sputter conditions with Kr ions and energies $\leqslant 2$ keV, ripple formation is observed only for higher incidence angles where the onset of ripple formation shifts to higher angle with increasing ion energy [46, 47]. The aim of this work is to make a comprehensive study of low-energy ion beam erosion of Ge with different noble gas ions (Ne, Ar, Kr and Xe) for a wide range

of experimental parameters. An overview of the evolving structures is given for the full angular range between 0° and 85°. The effect of ion species is studied for different ion energies ($\leqslant 2$ keV) as well as different time scales. All experiments are carried out in an experimental setup, which ensures negligible surface contamination with metallic or other impurities. The results are discussed in context to the recently proposed redistributive or stress-induced models for pattern formation. The experimental findings supported with TRIM.SP [48] simulations imply a strong correlation between the angular variation of sputter yield and formation of the surface pattern. The importance of gradient-dependent sputtering and the reflection of primary ions on pattern formation are shown. The angle-dependent sputter yield and the reflection coefficient are calculated for different ion species used in this work.

2. Experimental setup

The samples utilized in this work were commercially available: epi-polished Ge(100) substrate pieces (n-type) with a root-mean-square (rms) roughness of about 0.5 nm. These samples were mounted on a water-cooled substrate holder in a high vacuum chamber with a base pressure of 10^{-6} mbar. The substrate holder can be tilted from 0° (corresponding to normal ion incidence) up to 90° with respect to the axis of the ion beam source. Furthermore, the sample holder is equipped with a Si shielding in order to prevent metallic contaminations that affect the evolving structures [25, 31]. For that reason, the grid aperture of the ion source has been reduced compared to former experiments [45]. For the experiments a homebuilt Kaufman-type two grids ion source with a beam diameter of 100 mm is used. No iron or other metallic contaminations could be detected with Rutherford backscattering spectrometry as well as with x-ray photoelectron spectroscopy. This non-co-deposition setup [49] also prevents secondary collisions of scattered gas ions and re-deposition of sputtered silicon atoms. The current density was kept constant at 300 μA cm^{-2} during the experiments which results in an ion flux of $J = 1.87 \times 10^{15}$ cm^{-2} s^{-1} in a plane perpendicular to the ion beam. The surface topography was analyzed by scanning force microscopy (atomic force microscopy (AFM)) using a Dimension FastScan system from Bruker operating in TappingMode™ or ScanAsyst mode. The measurements were conducted in air using silicon nitride cantilever with a nominal tip radius smaller than 5 nm (TappingMode™) or 2 nm (ScanAsyst). The analyzed area of each sample was $2 \times 2\,\mu$m^2 or 4×4 and $10 \times 10\,\mu$m^2 with a resolution of at least 1024×1024 pixels.

3. Topography evolution under low-energy ion beam erosion on Ge

In the following part, the experimental results are shown which demonstrate the role of different control parameters on the topography evolution of Ge under low-energy ion beam erosion. In particular, the influence of ion incidence angle, ion species, ion energy and total ion fluence is examined in detail.

3.1. Overview of topography evolution versus ion incidence angle

Figure 1 shows the general influence of the incidence angle on the evolution of the surface topography. The irradiation, for example, with Kr^+ ions is shown with an ion energy of $E_{\text{ion}} = 1200$ eV and fluence of 6.7×10^{18} cm^{-2}.

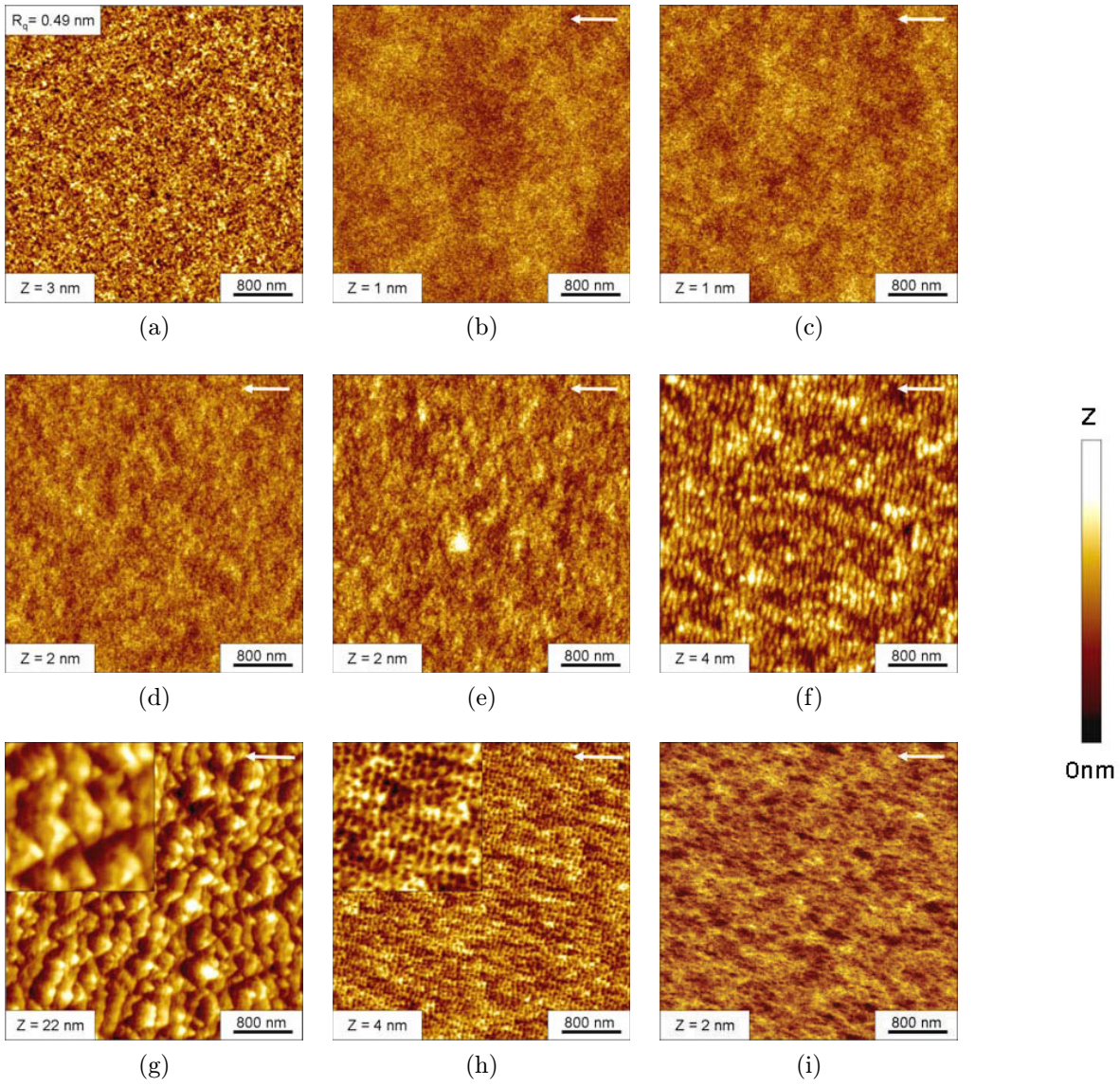

Figure 1. AFM images of the initial Ge surface (a) and Kr^+ ion beam eroded Ge surfaces for different ion incidence angles: $\alpha_{ion} = 0°$, 20°, 60°, 65°, 70°, 75°, 80° and 85° (b)–(i). The white arrow indicates the projection of the ion beam direction. The image size is 4×4 and $1 \times 1\ \mu m^2$ for magnification insets. The different height scales of the images are specified in each image. $E_{ion} = 1200\,eV$, $j_{ion} = 300\ \mu A\,cm^{-2}$ and ion fluence of $6.7 \times 10^{18}\,cm^{-2}$.

The first AFM image (figure 1(a)) shows the surface of the Ge substrate before erosion. The rms roughness R_q is approx. 0.5 nm. After normal incidence irradiation ($\alpha = 0°$, figure 1(b)) the surface is flattened and a very-low surface roughness of $R_q = 0.11$ nm is calculated. Up to an incidence angle of 60° (figure 1(d)) the roughness slightly increases to $R_q = 0.20$ nm, but it is still lower than the initial roughness of the Ge substrate. At 65° (figure 1(e)), the first signs of correlated surface structures emerge. These weakly pronounced structures have a preferential orientation perpendicular to the ion beam, but there is no regular pattern visible yet in both real

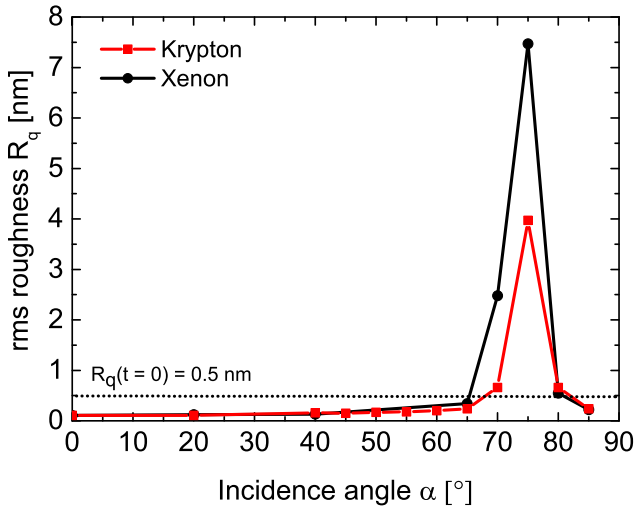

Figure 2. Root mean square roughness (rms) R_q as a function of ion incidence angle for Kr^+ and Xe^+ irradiated samples. $E_{ion} = 1200\,eV$, $j_{ion} = 300\,\mu A\,cm^{-2}$ and ion fluence of $6.7 \times 10^{18}\,cm^{-2}$. The dotted line indicates the initial roughness ($R_q(t = 0)$) of an untreated Ge wafer.

and Fourier space. The ripple pattern that evolves at 70° (figure 1(f)) is more pronounced. From the power spectral density (PSD) curve of the pattern, a wavelength of about 98 nm is obtained. From this, it can be concluded that in the case of 1200 eV Kr^+ ion beam erosion ripple formation starts at a critical angle between 65° and 70°. At 75°, (figure 1(g)), a saw tooth profile with an rms roughness of 4.0 nm is observed. The profile exhibits facets, forming a small angle of around 5° with respect to the global surface plane. This faceting is a clear indication that gradient-dependent sputtering dominates the surface evolution at this angle and this ion fluence. At an incidence angle of 80° (figure 1(h)), a mixture of a ripple-like and hole pattern is observed with a preferential orientation perpendicular to the ion beam direction and period of around 34 nm. This pattern is very similar to the fine structure found on top of the facets (downstream side) for 75° incidence angle. This behavior is caused by the increased local angle of incidence on top of the facets which is almost 80°. This pattern can be better ascertained at Xe-irradiated samples where larger facets evolve at 75°. At grazing incidence of 85° (figure 1(i)), only small structures are visible with a preferential direction parallel to the ion beam direction. Furthermore, the surface roughness decreases down to 0.24 nm. Figure 2 summarizes the evolution of the rms roughness as a function of ion incidence angle for Kr^+ and Xe^+ ion beam erosion. A maximum is clearly pronounced at 75° and an enhancement of the surface roughness in comparison to the initial surface is visible in the range of 70–80°. For all other ion incidence angles the rms surface roughness is smaller compared to the initial one, indicating a regime of surface smoothing.

3.2. Influence of ion species on pattern formation on Ge

Similar to the investigations presented in section 3.1, the surface evolution was examined over the whole range of incidence angles with respect to four different noble gas ion species (Ne, Ar, Kr and Xe). Apparently, the surface evolution is comparable for the case of Kr and Xe (see figure 2). Contrary to Kr (and Xe), where the surface destabilization is very pronounced

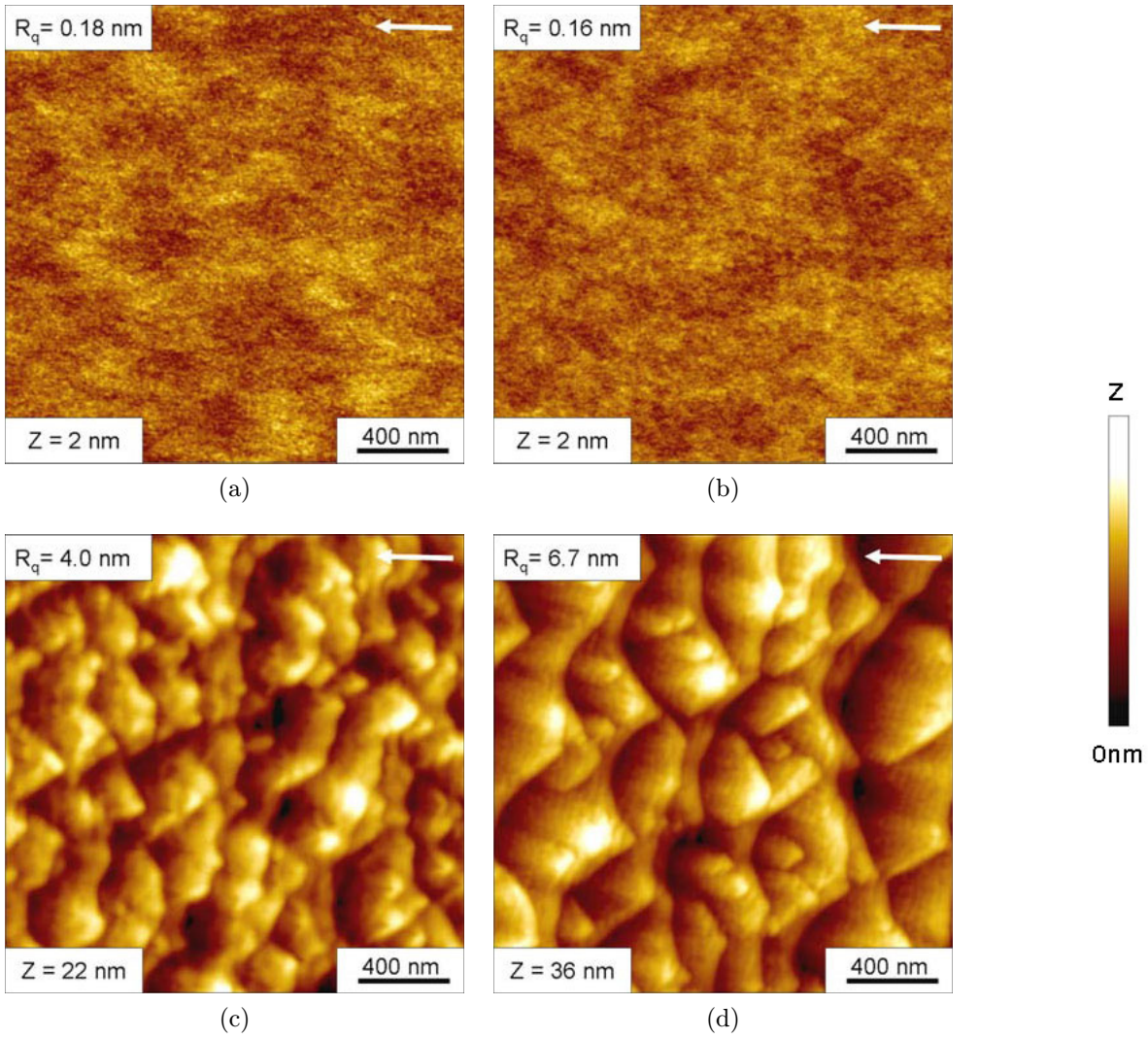

Figure 3. AFM images of ion beam eroded Ge surfaces with different ions: Ne (a), argon (b), Kr (c) and Xe (d). The image size is $2 \times 2\,\mu\text{m}^2$. The different height scales of the images and R_q values are specified in each image. The white arrow indicates the projection of ion beam direction. $E_\text{ion} = 1200\,\text{eV}$, $j_\text{ion} = 300\,\mu\text{A}\,\text{cm}^{-2}$ and ion fluence of $6.7 \times 10^{18}\,\text{cm}^{-2}$ at an ion incidence angle of $\alpha = 75^\circ$.

in a narrow range of incidence angles around 75° (see figure 2), the surface evolution behaves totally different for Ne and Ar irradiation. The topography evolution is compared for different ion species at 75° in order to illustrate the effect of ion species. Figure 3 shows the surfaces irradiated at an ion energy of $E_\text{ion} = 1200\,\text{eV}$ with a total fluence of $6.7 \times 10^{18}\,\text{cm}^{-2}$ for Ne, Ar, Kr and Xe ions.

In the case of Ne and Ar, no structures are observed (figure 3, top row). In fact, a smoothing effect of the surface occurs for both. Their surface roughness is smaller than the surface roughness of the initial Ge substrate ($R_\text{q} \approx 0.5\,\text{nm}$). As indicated in figure 3, the rms roughness decreases to 0.18 and 0.16 nm, respectively. A lower surface roughness for

Ar-ion-irradiated surfaces compared to Ne can also be observed for other incidence angles as well as for irradiation with larger ion energies (e.g. $E_{\mathrm{ion}} = 2000\,\mathrm{eV}$). This means that the surface generally becomes smoother after argon bombardment than for Ne irradiation. In contrast, there is a faceted topography evolving for Kr and Xe irradiation at 75° associated with a higher surface roughness. The single facets are larger in the case of Xe. As described in section 3.1, these facets form a small angle of around 5° with the global surface plane which results in a local ion incidence angle on top of the facets of around 80°. This induces a ripple-like fine structure on top of the facets with a mean period which is comparable with this evolving at an ion incidence angle of 80° after Kr or Xe irradiation. However, for Kr bombardment as shown in figures 1 and 3, it is hard to recognize due to the smaller facet size. Comparing Kr and Xe, the evolving structures and the general trend with the incidence angle are similar but the amplitude of the structures is higher in the case of Xe (see also figure 2).

3.3. Role of the ion energy on the topography evolution

This section describes the role of the ion energy E_{ion} on the pattern formation. The ion energy is varied between 400 and 2000 eV, which is limited by the used ion beam source and power supply. The samples were eroded with Xe^+ ions at incidence angles of 65° as well as 75° with a total fluence of $6.7 \times 10^{18}\,\mathrm{cm}^{-2}$. The corresponding AFM images are presented in figures 4 and 6.

In particular, the angle of 65° (figure 4) was chosen to have a closer look at the transition regime between smoothing and roughening which takes place around this value. Furthermore, the largest structures evolve around 75° (figure 6) where the sputter yield has a maximum. A highly regular ripple pattern evolves for the lowest energy (400 eV) at 65° (figure 4(a)). The ripples are oriented perpendicular to the ion beam direction (i.e. ripple wave vector is parallel to ion beam projection) with a wavelength slightly above 30 nm. This regular pattern is superimposed by long wavelength triangular and faceted hillocks and depressions. Along these structures the ripples are curved and the wavelength of the ripples slightly changes from the upstream to the downstream side depending on the local surface angle. This is illustrated in the magnified 400 eV image (figure 4(e)). For an ion energy of 800 eV (figure 4(b)), the ripple wavelength increases to approx. 52 nm and the amplitude of the ripples decreases compared to 400 eV that correlates with a smaller rms value, indicated in the top left corner of the image. In addition, the pattern for 800 eV becomes more irregular. If the ion beam energy increases further, the ripple pattern vanishes and rudiments of a pattern are visible only. The reduction of surface amplitude fluctuation is also seen from the lower rms roughness values, where the smallest roughness is observed for 2000 eV (figure 4(d)). Furthermore, no signs of a pattern are visible in the AFM images as well as in the Fourier analysis. The overall behavior is also demonstrated in figure 5 where the PSD curves are plotted for the AFM images from figure 4. It is clearly seen that the wavelength shifts to larger values (smaller spatial frequencies, indicated by the arrows) and the ripple regularity decreases with increasing ion energy, which can be observed from broader peaks and suppression of higher-order peaks in figure 5. It is obvious that the roughness decreases over the whole spatial frequency range encompassed by the AFM measurements.

The second series of experiments has been done at an ion incidence angle of 75°, whereas other ion beam parameters were the same as for the series described before. The experimental results are summarized in figure 6. At this angle of incidence saw tooth profiles with rms

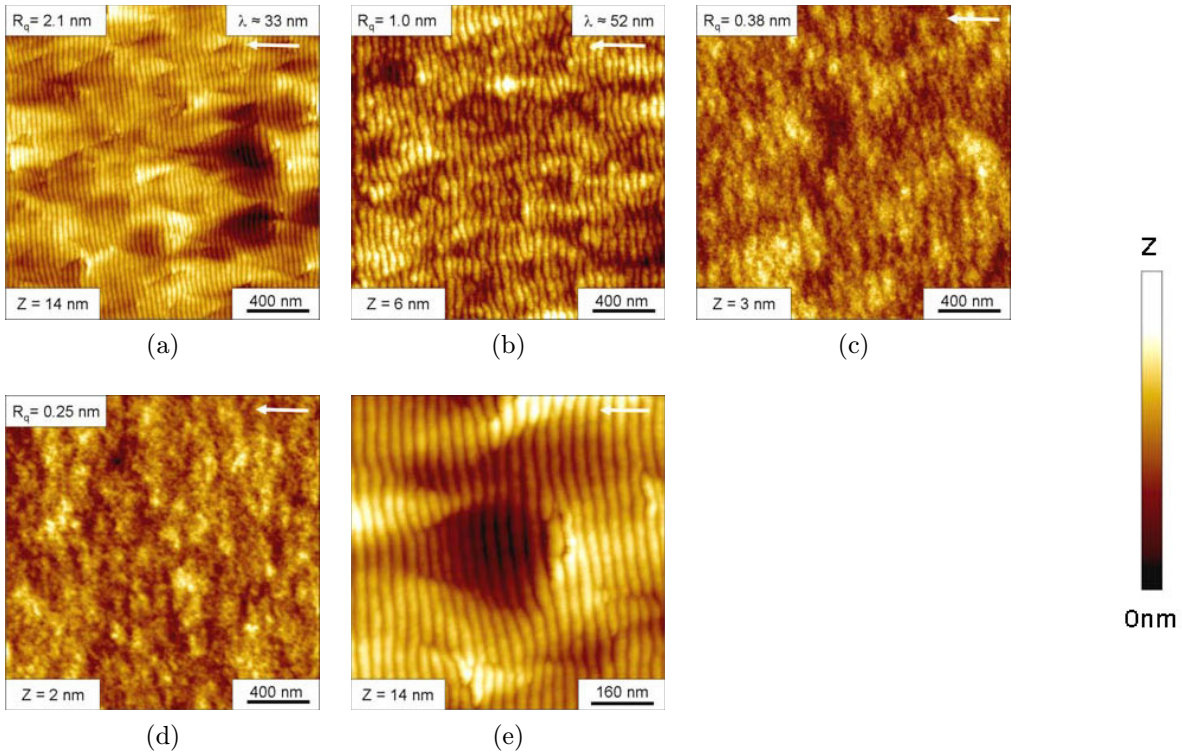

Figure 4. AFM images of Xe^+ ion beam eroded Ge surfaces with different ion beam energies: 400, 800, 1200 and 2000 eV (a)–(d). The image size is $2 \times 2\,\mu m^2$ and $800 \times 800\,nm^2$ for the magnification of the 400 eV sample (e). The different height scales of the images are specified in each image. The white arrow indicates projection of the ion beam direction. Ion incidence angle of $\alpha = 65°$, $j_{ion} = 300\,\mu A\,cm^{-2}$ and ion fluence of $6.7 \times 10^{18}\,cm^{-2}$.

roughness values between 6 and 8 nm evolve for all used ion energies, similar to the pattern seen for Kr^+ ion erosion of Si [25]. The topographies show extended facets at the downstream side and the angle of the local surface normal toward the global surface normal is determined to be 5°. For increasing ion energy the size of the facets shrink and the topography is more redolent of a faceted ripple pattern. As described in section 3.2 the downstream facets are decorated by a sub-pattern which can be understood again by the enlarged local incidence angle on the facets. From the magnified amplitude error images (figures 6(d)–(f)) it can be seen that the period and amplitude become more pronounced with increasing ion energy.

3.4. Temporal evolution of surface pattern

The last set of experiments focused on the time evolution of the surface pattern. Among the different parameter regimes that have been investigated two time series will be shown. In the first case, $E_{ion} = 600\,eV$ and an incidence angle of 65° were chosen where ripple formation occurs (see figure 4). The second set of experiments was conducted using 1200 eV Xe ions and an incidence angle of 75°, a regime where significant faceting appears (see figure 6). The samples were irradiated for durations from 1 up to 120 min that corresponds to a fluence range

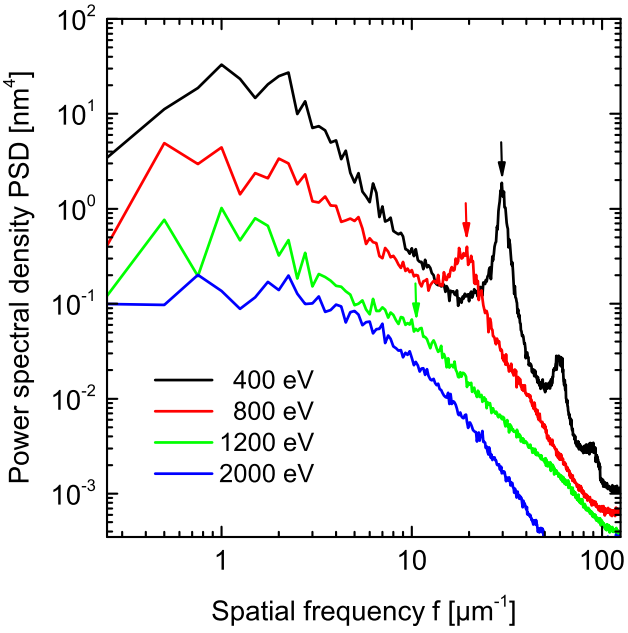

Figure 5. Calculated PSD from AFM images of Xe^+ ion beam eroded Ge surfaces with different ion beam energies from 400 to 2000 eV. Ion incidence angle of $\alpha = 65°$, $j_{ion} = 300\,\mu A\,cm^{-2}$ and ion fluence of $6.7 \times 10^{18}\,cm^{-2}$.

of 1.12×10^{17}–$1.35 \times 10^{19}\,cm^{-2}$. Some characteristic AFM images of the ripple pattern formed at 65° for different ion fluences are shown in figure 7.

From these images, several important points can be noted. It is clearly seen that ripple pattern changes with fluence. The amplitude and regularity of the ripple pattern increase with time. Furthermore, larger wavelength structures, i.e. larger triangular and faceted hillocks and depressions become more and more evident. This is also observed from the PSD curves in figure 8 calculated from $4\mu m \times 4\,\mu m$ AFM images.

In the PSD curves, two distinct frequency ranges can be identified. In the low spatial frequency region ($f \leqslant 10\,\mu m^{-1}$, corresponding to spatial wavelengths $\geqslant 100$ nm) the roughness grows rapidly with fluence as seen as hillocks and depressions in the AFM images. Moreover, a high-frequency peak which correlates with the ripple pattern is evident. Beginning with the smallest adjustable fluence the associated peak shifts to lower frequencies (larger ripple wavelengths) with increasing erosion time. The arrows in figure 8 mark the ripple wavelength and the dotted lines indicate the peak positions (wavelength) at smallest and largest ion fluences, respectively. It is further evident that the width of the peaks decreases with the ion fluence correlating with a higher regularity of the pattern. These experimental findings are summarized in figure 9, which shows the temporal evolution of the surface roughness and ripple wavelength for more than two orders of magnitude varying ion fluence (or erosion time).

As is already expected from the PSD curves, R_q and λ grow non-exponentially with time. It should be noted that for ion fluences less than or equal to $1.12 \times 10^{18}\,cm^{-2}$, the presented data are averaged over two independent experimental runs, where the individual runs show a variation in surface roughness and ripple wavelength $\leqslant 5\%$ related to the averaged values.

Finally, the evolution of faceted pattern at 75° with ion fluence will be addressed. Characteristic AFM images taken after erosion with different fluences are presented in figure 10.

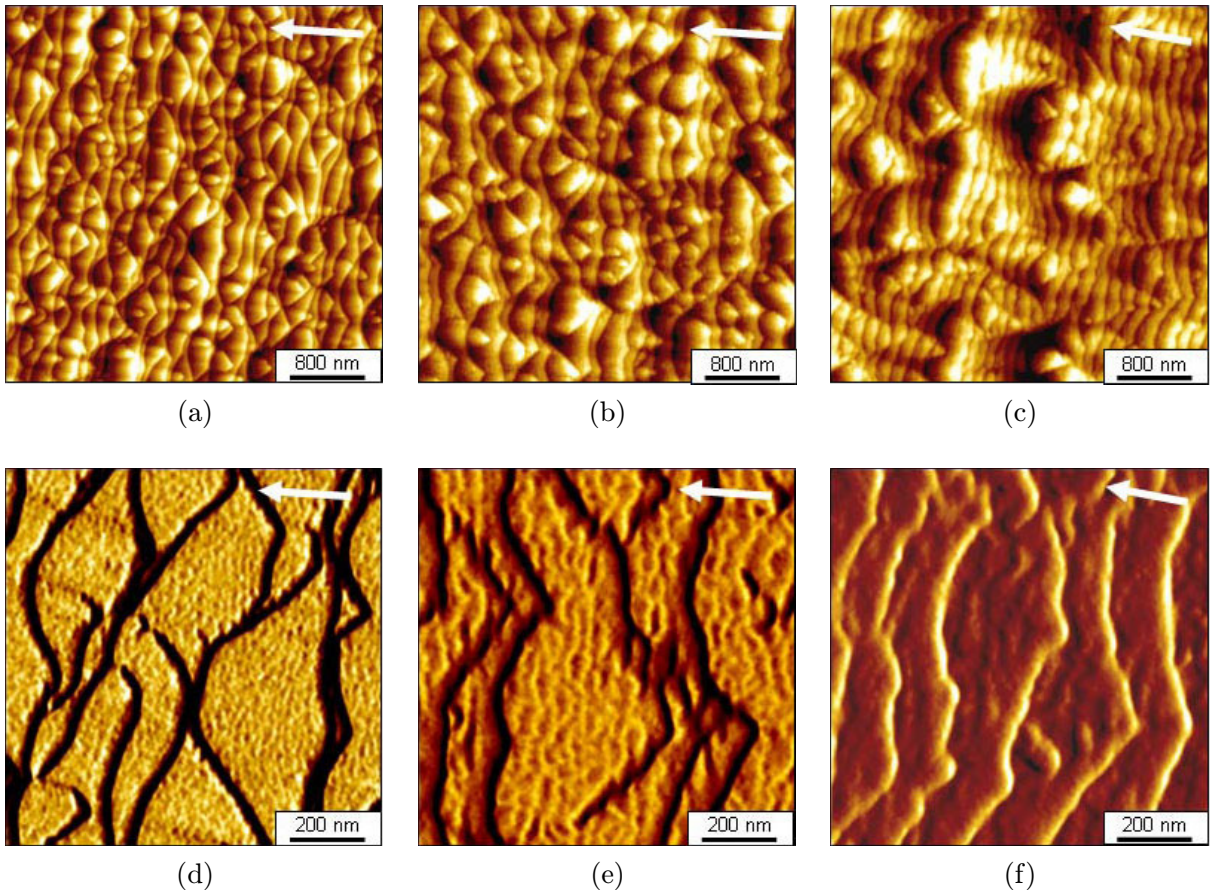

Figure 6. AFM images of Xe^+ ion beam eroded Ge surfaces with ion energies $E_{ion} = 400$, 1200 and 2000 eV (a)–(c). The image size is $4 \times 4\,\mu m^2$. The white arrow indicates projection of the ion beam direction. Images (d)–(f) are magnified amplitude error images ($1 \times 1\,\mu m^2$) showing more details of the sub-pattern on the larger facets for $E_{ion} = 400$, 1200 and 2000 eV, respectively. Ion incidence angle of $\alpha = 75°$, $j_{ion} = 300\,\mu A\,cm^{-2}$ and ion fluence of $6.7 \times 10^{18}\,cm^{-2}$.

It is noticed that the pattern after the shortest irradiation time (figure 10(a)) shows a ripple-like appearance with wavelength of approx. 42 nm and the regularity is less than that for the corresponding case at 65°. With increasing fluence the structures are subjected to a strong coarsening (i.e. smaller ones disappear while larger ones grow). Furthermore, the pattern becomes more and more faceted and again the downstream sides of the faceted structures form an angle of 5° (± 0.5°) toward the global surface plane (as already addressed in Section 3.1). If the fluences are high enough ($\geqslant 3.37 \times 10^{18}\,cm^{-2}$), a sub-pattern emerges at the downstream side of the facets with a ripple wavelength of approx. 45 nm, similar to the pattern formed at 80° incidence angle at plane surfaces (figure 1), which is clearly visible in the AFM image for a fluence of $1.35 \times 10^{19}\,cm^{-2}$ (figure 10(f)). The quantitative evolution of the surface roughness and ripple wavelength/facet size is summarized in figure 11.

Both quantities exhibit a non-exponential growth, as is already observed in the case of 65° ion incidence angle (figure 9). Considering the time evolution of the pattern at 65° and

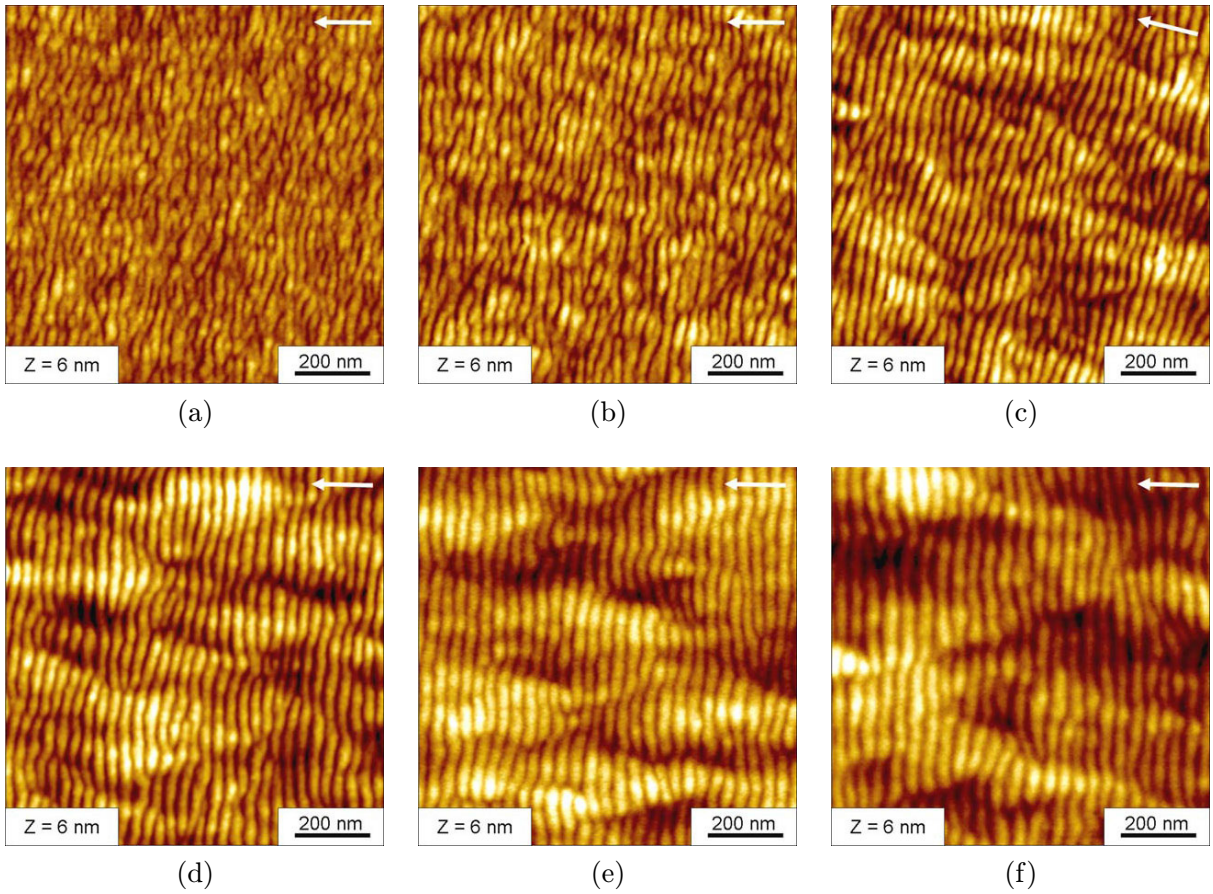

Figure 7. AFM images of Xe^+ ion beam eroded Ge surfaces for different fluences: $\Phi = 1.12 \times 10^{17}\,\mathrm{cm}^{-2}$ (a), $2.25 \times 10^{17}\,\mathrm{cm}^{-2}$ (b), $5.62 \times 10^{17}\,\mathrm{cm}^{-2}$ (c), $1.12 \times 10^{18}\,\mathrm{cm}^{-2}$ (d), $3.37 \times 10^{18}\,\mathrm{cm}^{-2}$ (e) and $1.35 \times 10^{19}\,\mathrm{cm}^{-2}$ (f). The image size is $2 \times 2\,\mu\mathrm{m}^2$. The height scale of each image is 6 nm. The white arrow indicates projection of the ion beam direction. $E_{\mathrm{ion}} = 600\,\mathrm{eV}$, $j_{\mathrm{ion}} = 300\,\mu\mathrm{A\,cm}^{-2}$ and ion incidence angle of $\alpha = 65^\circ$.

75° (figures 9 and 11), two interesting points should be emphasized. At 75° the rms roughness increases almost by factor 10 from the lowest to the highest fluence interval, in contrast to 65° incidence angle where the roughness is only doubled in the corresponding fluence interval. In addition, the pattern coarsening is drastically reduced at 65° ion incidence from $\lambda \approx 31$ to 42 nm. In the case of 75° the mean size of the ripples/faceted structures increases more than one order of magnitude from 42 to approx. 700 nm.

4. Discussion

4.1. Comparison of results to former reports on pattern formation

Compared to previous investigations [45, 50] it is apparent that in the present study no ripple and dot pattern have been encountered at low incidence angles. In the modified experimental setup used here (see section 2), no simultaneous co-deposition of iron takes place. As is recently

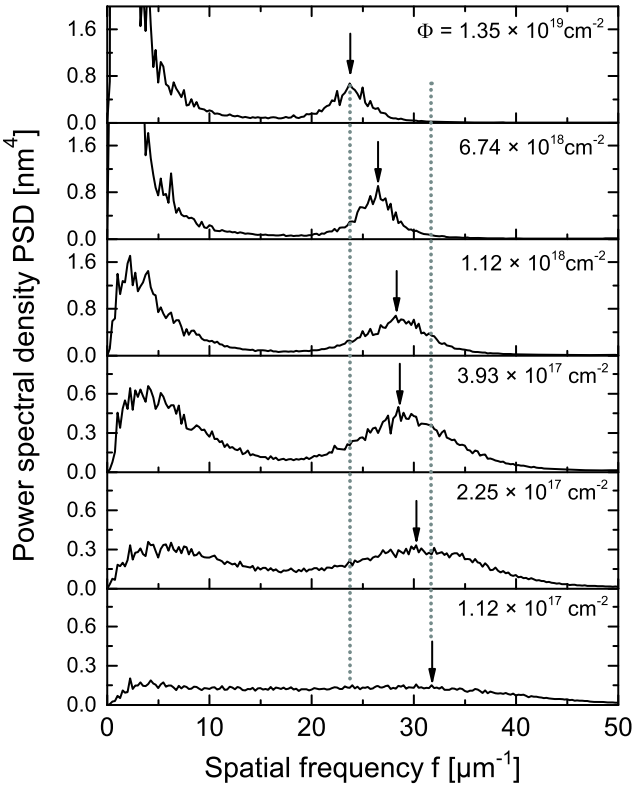

Figure 8. Calculated PSD of images of Xe^+ ion beam eroded Ge surfaces for fluences from $\Phi = 1.12 \times 10^{17}$ up to $1.35 \times 10^{19}\,\mathrm{cm}^{-2}$. $E_{\mathrm{ion}} = 600\,\mathrm{eV}$, $j_{\mathrm{ion}} = 300\,\mu\mathrm{A\,cm}^{-2}$, ion incidence angle of $\alpha = 65^{\circ}$. The dotted vertical lines mark the ripple wavelength for lowest and largest fluence, respectively.

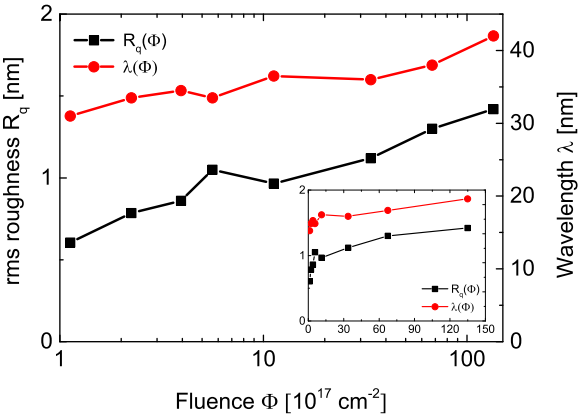

Figure 9. Root mean square roughness (rms) and structure wavelength as a function of fluence for Xe^+ irradiated samples. $E_{\mathrm{ion}} = 600\,\mathrm{eV}$, $j_{\mathrm{ion}} = 300\,\mu\mathrm{A\,cm}^{-2}$, ion incidence angle of $\alpha = 65^{\circ}$ and ion fluence from $\Phi = 1.12 \times 10^{17}$ to $1.35 \times 10^{19}\,\mathrm{cm}^{-2}$.

shown for the ion erosion of Si [25, 26, 31, 32] the insertion of silicide-forming metals is essential for the pattern formation at low incidence angles. In the same way, it is evident that iron incorporation is likewise the key factor for the formation of highly regular pattern on Ge at

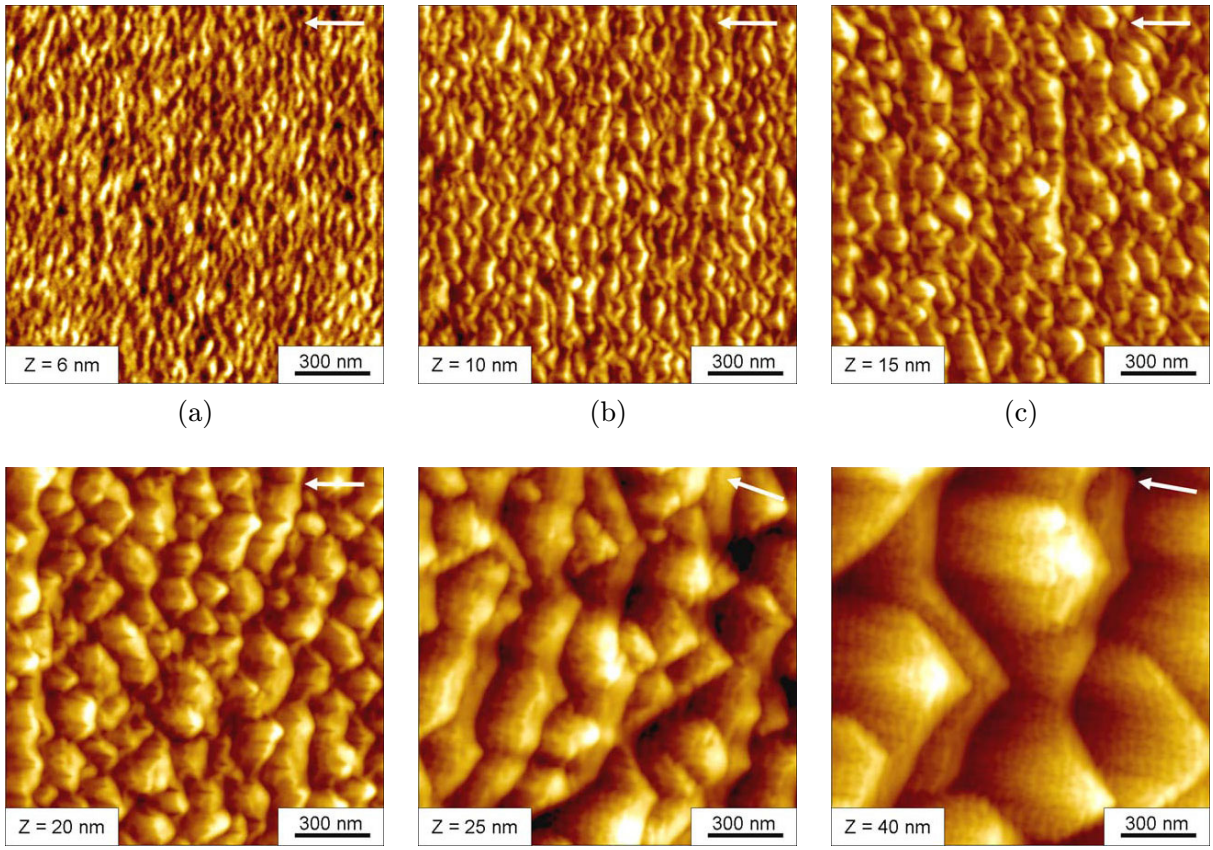

Figure 10. AFM images of Xe^+ ion beam eroded Ge surfaces for different fluences: $\Phi = 1.12 \times 10^{17}\,\mathrm{cm}^{-2}$ (a), $2.25 \times 10^{17}\,\mathrm{cm}^{-2}$ (b), $5.62 \times 10^{17}\,\mathrm{cm}^{-2}$ (c), $1.12 \times 10^{18}\,\mathrm{cm}^{-2}$ (d), $3.37 \times 10^{18}\,\mathrm{cm}^{-2}$ (e) and $1.35 \times 10^{19}\,\mathrm{cm}^{-2}$ (f). The image size is $1.5 \times 1.5\,\mu\mathrm{m}^2$. The different height scales of the images are specified in each image. The white arrow indicates projection of the ion beam direction. $E_{\mathrm{ion}} = 1200\,\mathrm{eV}$, $j_{\mathrm{ion}} = 300\,\mu\mathrm{A\,cm}^{-2}$, ion incidence angle of $\alpha = 75^\circ$.

normal or low ion incidence conditions. If the formation of iron germanides is not possible, as in the present experiments, surface smoothing occurs.

In the following part the presented results, selected from a comprehensive study varying the control parameters ion species, ion energy, ion incidence angle and erosion time will be set within the context of recently published investigations of Kr^+ ion beam erosion of Ge under partially comparable experimental conditions [46, 47]. Both studies focused on the linear regime of pattern formation at rather low ion fluences.

In the first study by Anzenberg *et al* [46], the kinetics of surface evolution of pre-smoothed and pre-rippled Ge under 1 keV Kr ion irradiation for selected incidence angles was examined. The pre-patterning with 500 eV Kr using a broad beam ion source at an incidence angle of 60° results in a ripple wavelength of approx. 45 nm as unfortunately no ion fluence was specified. This is consistent with a ripple wavelength between 32 and 42 nm observed for 65° ion erosion with 600 eV Xe (figure 9) even considering the growth of wavelength near the critical angle. Furthermore, it can be concluded that the critical angle in this study is below 60°. For 1 keV

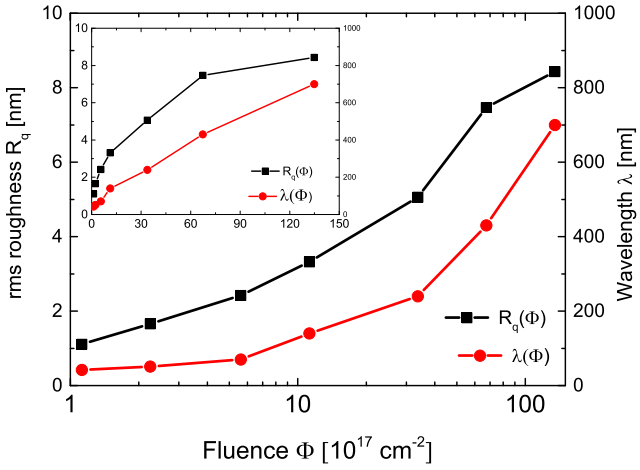

Figure 11. Rms and structure wavelength as a function of fluence for Xe^+ irradiated samples. $E_{ion} = 1200\,eV$, $j_{ion} = 300\,\mu A\,cm^{-2}$, ion incidence angle of $\alpha = 75°$ and ion fluence from $\Phi = 1.12 \times 10^{17}$ to $1.35 \times 10^{19}\,cm^{-2}$.

Kr ions erosion of pre-smoothed surfaces at 75° with another ion source a wavelength of approx. 60 nm can be deduced from grazing-incidence small-angle x-ray scattering (GISAXS) measurements presented in [46], which is again comparable to the value obtained in the presented experiments for the smallest ion fluences (figure 11). From a fit to the experimental dispersion GISAXS data Anzenberg *et al* derived the curvature-dependent coefficients as a function of ion incidence angle with stability to instability transition at 62°. The authors were not sure whether the difference of the critical angle determined for 500 eV results from the different ion energy or from the different experimental setup. Our results illustrated in figures 4 and 5 clearly show that the transition angle (i.e. where ripples starts to form) shifts to lower angles with decreasing ion energies.

In a related study of Perkinson *et al* [47], using the same ion beam facilities as for pre-patterning in the former case, pattern formation at 250 and 500 eV Kr ion erosion was investigated for an ion incidence angle interval ranging from 0° to 80°. From the associated phase diagram, the authors deduced a critical angle of 57.5°, separating surface smoothing from pattern formation. This validates again the observed trend that the critical angle decreases as ion energy becomes smaller, as it can be seen in figures 4 and 5. At an incidence angle of 75°, a hole pattern is reported by Perkinson *et al*, similar to the sub-pattern shown in figure 1 for $E_{ion} =$ 1200 eV and 80° incidence angle. The sub-pattern can be observed also on the downstream side of the evolving facets at $\alpha = 75°$ (figures 3, 6 and 10), where the local incidence angle is approx. 80° as discussed in sections 3.2 and 3.3. This gives evidence that not only the critical angle shifts to larger values with increasing ion energy, but the whole regime of pattern moves to large incidence angles (also seen in figure 6). In addition, the reported wavelengths in [47] are comparable to the wavelength at 400 or 600 eV in this work (e.g. figures 5 and 9). Slightly different from our investigations a ripple amplitude saturation for fluences $\geqslant 1.8 \times 10^{17}\,cm^{-2}$ (at least up to fluences of $1.8 \times 10^{18}\,cm^{-2}$) was observed. Also, the larger ripple wavelength at 250 eV compared with 500 eV for an incidence angle of 60° (see table 1 in [47]) cannot be seen. Finally, it should be mentioned that our figures 9 and 11 substantiate the observation of Perkinson *et al* that the growth rates of surface amplitudes/roughness increase as the incidence angle is shifted to a larger value with respect to the critical angle.

Table 1. Calculated mean depth a as well as longitudinal and lateral straggling parameters σ and μ for the deposited energy distribution for different ion and energies. The energy distributions were obtained from the distribution of displaced atoms (vacancies, recoils) calculated by SRIM2012.

	a (nm)	σ (nm)	μ (nm)
Neon/$E_{\text{ion}} = 1200\,\text{eV}$	2.39	1.82	1.70
Argon/$E_{\text{ion}} = 1200\,\text{eV}$	1.87	1.32	1.10
Krypton/$E_{\text{ion}} = 1200\,\text{eV}$	1.83	1.13	0.83
Xenon/$E_{\text{ion}} = 1200\,\text{eV}$	1.86	1.05	0.72
Xenon/$E_{\text{ion}} = 500\,\text{eV}$	1.23	0.68	0.58
Xenon/$E_{\text{ion}} = 1000\,\text{eV}$	1.70	0.97	0.70
Xenon/$E_{\text{ion}} = 1500\,\text{eV}$	2.07	1.18	0.72
Xenon/$E_{\text{ion}} = 2000\,\text{eV}$	2.35	1.37	0.91

4.2. Discussion of pattern formation with recent models

In the discussion of experimental results, both groups [46, 47] conclude that in the case of Kr ion erosion of Ge, the CV-model [34] as well as the modified by Madi *et al* [35] give the proper qualitative behavior; however, they fail to predict qualitatively the observed critical angle which significantly differs from the expected value of 45°.

In the presented experiments, a wider range of parameters has been included compared to [46, 47]. In order to see if there are further potential conflicts with the simplified mass redistribution model, we follow Madi's approach [35] and calculate the curvature-dependent coefficients S_x for all ion/Ge-target combinations as well as for different ion energies E_{ion} relevant to the experiments. However, deviating from the calculation method proposed by Madi *et al*, some modifications have been made in the calculation of the erosive (S_x^{eros}) and redistributive parts (S_x^{distr}) of the curvature-dependent coefficients ($S_x = S_x^{\text{eros}} + S_x^{\text{distr}}$). For the calculation of the mean depth a and the longitudinal σ and lateral μ straggling parameters of the deposited energy distribution, required for determination of the Bradley–Harper coefficients Γ_x and Γ_y, the approach of Bolse [51] was used. In this approach the distribution of displaced atoms (vacancies, recoils) is used to deduce the distribution of the deposited energy. The vacancy/recoil distribution is extracted from the collision.txt output file calculated by SRIM2012 [52] and analyzed assuming a Gaussian distribution. Recently, an alternative method for the estimation of these parameters is proposed by Bobes *et al* [53]. The calculated parameters a, σ and μ are given in table 1 for 1200 eV Ne, Ar, Kr, Xe and for various energies with Xe. Usually, the determined values are smaller than the values calculated from ion range distributions [35]. In addition, the sputter yield curves are obtained from TRIM.SP [48] because there are some discrepancies in the calculation of sputter yields with former versions of SRIM [54]. For the TRIM.SP simulations 250 000 ion impacts are simulated to ensure a sufficiently good statistic. Furthermore, the potentials and free parameters that have been suggested by Eckstein [55] are used. The ion energy-dependent mean displacement distance of target atoms δ, required for the calculation of the redistributive part, is determined from the expressions in [56]. The calculated curvature-dependent coefficients are summarized in

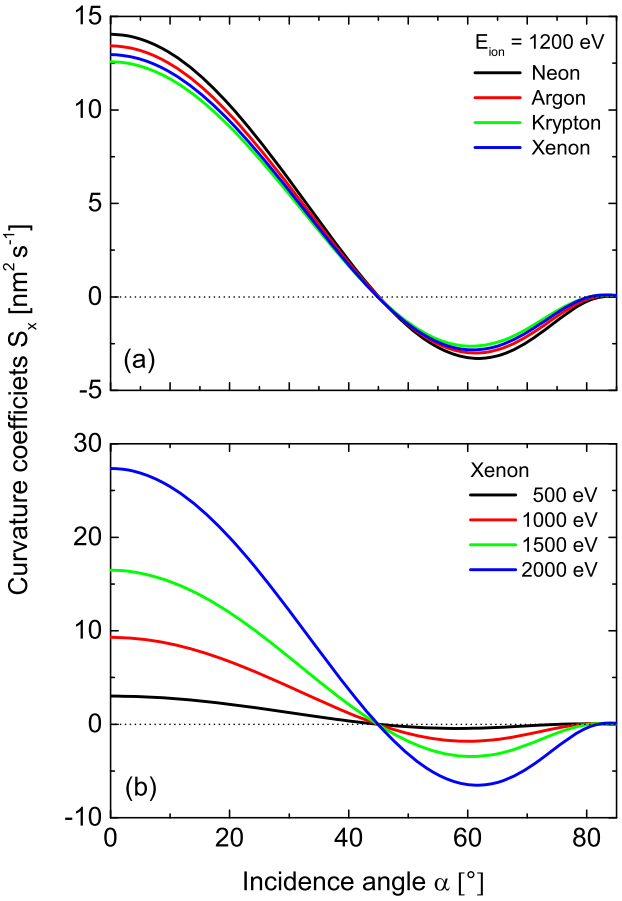

Figure 12. Calculated curvature coefficients for different ion species with $E_{\mathrm{ion}} = 1200\,\mathrm{eV}$ (a) and different ion energy for Xe (b) (ion flux $J = 1.87 \times 10^{15}\,\mu\mathrm{A\,cm^{-2}\,s^{-1}}$). The ion energy-dependent mean displacement distance of target atoms was $\delta_{500\,\mathrm{eV}} = 22\,\mathrm{nm}$, $\delta_{1000\,\mathrm{eV}} = 54\,\mathrm{nm}$, $\delta_{1200\,\mathrm{eV}} = 69\,\mathrm{nm}$, $\delta_{1500\,\mathrm{eV}} = 93\,\mathrm{nm}$ and $\delta_{2000\,\mathrm{eV}} = 136\,\mathrm{nm}$.

figure 12 for 1200 eV Ne, Ar, Kr and Xe on Ge (a), and 500, 1000, 1500 and 2000 eV Xe on Ge (b). The values used for δ are given in the figure caption.

Independently of ion species and energy, both curves in figure 12 show qualitatively the expected shape, i.e. a transition from stability (smoothing) to instability (parallel mode ripple) at an incidence angle of approx. 45° which is inherent to the simplified approach for the redistributive part. Small deviations from 45° are caused by the contribution from the erosive part. Therefore, ripple pattern should occur irrespective of ion species, which contradicts the lack of ripple formation for Ne and Ar ions. In addition, the onset angle of ripple formation (Kr, Xe) significantly differs from 45° (figures 1 and 4). The shift of critical angle with ion energy (figures 4 and 5) is also not reproduced from figure 12(b). Furthermore, the expected ripple growth rate should increase with S_x (and energy according to figure 12(b)), which is again not seen (figures 4 and 5). One further conclusion from the mass redistribution models is the diverging ripple wavelength in the vicinity of the angular region that separates instable (pattern forming) from stable (smoothing) surface evolution. From the presented investigations and from a set of similar investigations for Si, fused silica and sapphire [57] no evidence of a

diverging wavelength in the vicinity of the critical angle is observed. Solely a moderate increase of ripple wavelength can be seen accompanied with a decline of ripple amplitude and pattern regularity.

At this point it is not clear if the crater function approach by Norris *et al* [38] gives a more realistic picture compared to the simplified CV/Madi [35] model because of lack of supporting MD simulations. Thus, it is still an open question whether the absence of pattern formation for Ne and Ar ions can be attributed to redistributive processes. However, based on the similarity of the basic mechanisms of ion–target interaction a completely different behavior is not expected for Ne, Ar from one side and Kr, Xe from the other side. Therefore, from the presented results it appears that mass redistribution alone cannot describe the observed scenarios for pattern formation on Ge.

In this context, it should also be mentioned that recently proposed models based on ion-induced solid flow [39, 41] fail to explain the experimental observation. Both approaches predict a critical angle of 45°, in coincidence with experimental results for Ar ion erosion of Si [40, 58], and a diverging wavelength at this angle. In both models this is the direct consequence of the implemented angular dependence of the stress tensor [41] or the proportionality of the so-called body force to the local ion flux at the surface [39]. As noted by Norris [41] this proportionality could be no longer valid for higher incidence angles. At high incidence angles, the amount of reflected ions increases, which could change the angular dependence of the stress tensor. But it is again not clear if a modified angular dependence of the stress tensor could explain the completely different surface evolution under inert gas ion erosion of Ge.

4.3. Role of surface-gradient-dependent sputtering and reflection of primary ions

From the experiments can be concluded that an evidence for coarsening (e.g. figures 7–11) and faceting (e.g. figures 1–3 and 6) of surface pattern starting already at low fluences exists. Both observations indicate that gradient-dependent sputtering and reflection of primary ions play crucial role, just at the earliest accessible stage of surface evolution. As was mentioned above, sputtering and the reflection of ions for all possible ion/target combinations were analyzed with TRIM.SP simulation tool. From these calculations it is found that the amount of reflected ions naturally increases with ion incidence angle. Otherwise the amount of reflected ions for a given incidence angle increases for lower energies and also for ions with a lower mass. For example, approx. 1/3 of all Xe^+ ions at 65° incidence angle and $E_{ion} = 600\,eV$ are reflected. This number increases to 3/5 for $E_{ion} = 1200\,eV$ and an incidence angle of 75°. In conjunction with the Hauffe mechanism [59], this accounts for the reduced ripple coarsening seen in figure 9 (Xe^+, 65°, 600 eV) compared to figure 11 (Xe^+, 75°, 1200 eV). In the Hauffe model coarsening of structures is attributed to reflected ions impinging adjoining structures. The local erosion rate is enhanced in the vicinity of larger structures as more particles are reflected from larger structures than from smaller ones. Consequently, smaller features close to the larger ones vanish and the surface coarsens. This effect strongly enhances at larger incidence angles, as already seen on SiO_2 surfaces [60].

Additionally, the angular dependence of the normalized sputter yields (normalized to their values at normal incidence) and the normalized deposited energy for all four ions with 1200 eV were extracted from TRIM.SP simulations and plotted in figures 13(a) and (b). Likewise the deposited energy, which is calculated from total energy of all incoming ions subtracting the total energy of all reflected and sputtered ions/atoms, was also normalized to the value at normal incidence. From figure 13(a) it is obvious that the angular variation of the sputter yield

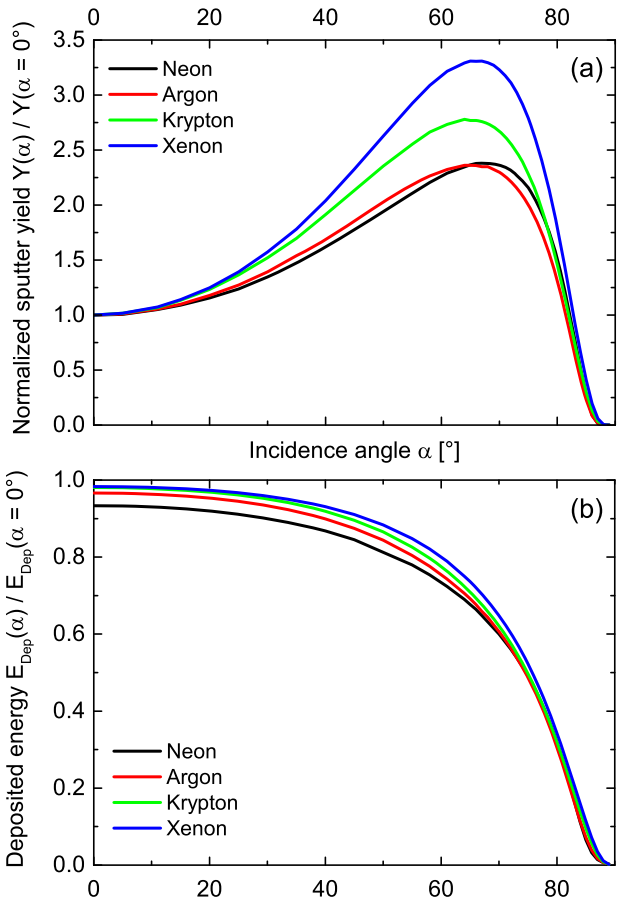

Figure 13. Normalized sputter yields $Y(\alpha)/Y(0^\circ)$ (a) and deposited energy $E_{\mathrm{dep}}(\alpha)/E_{\mathrm{dep}}(0^\circ)$ (b) for different ion species at ion energy $E_{\mathrm{ion}} = 1200\,\mathrm{eV}$ obtained from TRIM.SP calculations.

is more pronounced for Kr or Xe ions compared with Ne or Ar. Consequently, the difference in the amplification rate of two adjacent surface elements with different local surface slopes is higher for Kr and Xe irradiation as for Ar or Ne. In contrast, nearly the same quantitative curve shape for the deposited energy is obtained. This is due to the fact that for heavier ion masses less ions (and energy) are reflected but more atoms are sputtered. For lighter ions the reverse scenario is found. It should be underlined that these findings correlate with recent MD simulations of the deposited energy distribution and sputtering of Si and Ge by Hossain *et al* [61] The authors could validate the assumption of an ellipsoidal energy distribution as in Sigmund theory of sputtering [62]; however, the linear relationship between local sputter yield and local deposited energy as supposed by the BH model [33] is not valid. Nevertheless the overall deposited energy decreases with incidence angle (figure 13(b)), the local surface-deposited energy grows with the incident angle, up to the angle, where the sputter yield has maximum, is reached [61]. At oblique ion incidence the ellipsoid of the deposited energy is inclined to the surface and the center of the distribution is closer to the surface. Nevertheless, the angular increase of surface-deposited energy is significantly lower than the angular variation of sputter yield [61]. In figures 14(a) and (b) the angular curves of sputter yield and energy distribution were calculated for the 'limiting cases' of the experiments: lowest (400 eV) and

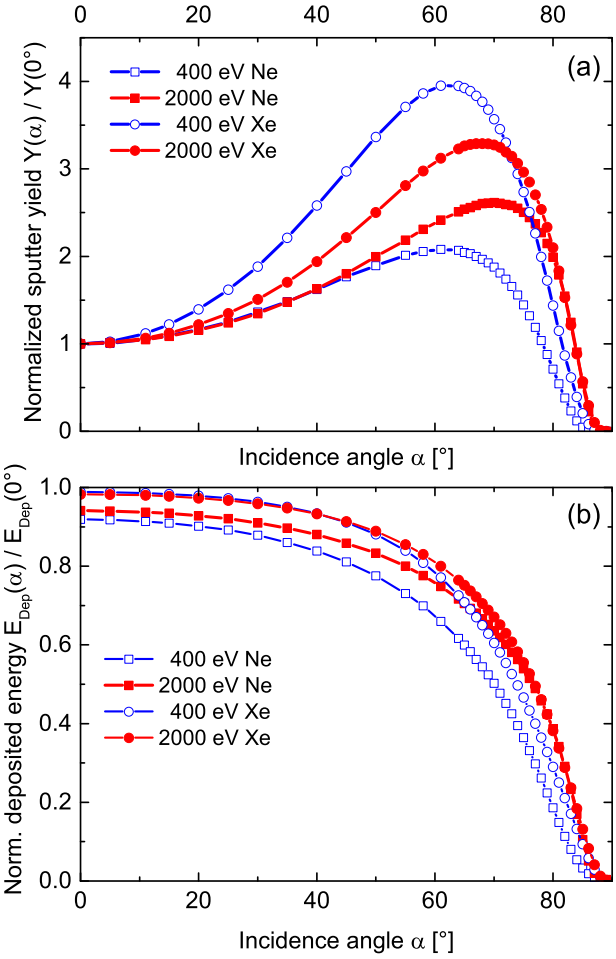

Figure 14. Normalized sputter yields $Y(\alpha)/Y(0^\circ)$ (a) and deposited energy $E_{\mathrm{dep}}(\alpha)/E_{\mathrm{dep}}(0^\circ)$ (b) for Ne and Xe at ion energies of $E_{\mathrm{ion}} = 400$ and 2000 eV obtained from TRIM.SP calculations.

highest (2000 eV) ion energy and lightest (Ne) and heaviest (Xe) ion. Typically, the normalized total deposited energy (figure 14(b)) is smaller at lower ion energies due to the higher reflection coefficient at these energies. For larger incidence angles and higher ion energies the difference becomes smaller. Thus, comparable angular variations of the surface-deposited energy are expected independent of E_{ion} and ion mass as can be seen in table 1.

However, large variations in the sputter yield curves in figure 14(a) are seen again. In general, the angular variations for Xe ions are much larger compared to Ne. For Xe the maximum in sputter yield shifts to lower angles with decreasing energy. The same tendency is observed for Ne, but here the angular variation $Y(\alpha)/Y(0^\circ)$ grows at higher energies in contrast to Xe. Figure 14(a), together with figures 3 and 4 implies that pattern formation is strongly influenced by the angular variation in sputter yield. It seems that if the variation is too small no ripples or surface structures are formed. The model calculations of sputtering and reflection in conjunction with the experimental results (showing structure coarsening and faceting) indicate that gradient-dependent sputtering together with reflection of ions significantly contribute to the surface evolution at least for the studied experimental conditions (ion/target combinations,

incidence angles, ion energies and ion fluences). Already for angles near the onset of pattern formation (approx. 65°, dependent on ion energy) and earliest erosion time or fluences (approx. 1 min or 10^{17} cm^{-2}) these mechanisms can affect the pattern formation. One should be aware that both processes give a nonlinear and a non-local contribution to the pattern-forming mechanism. In this context it is interesting to note that no clear evidence for diverging wavelengths is seen in experiments, as only a moderate growth of wavelength approaching the transition angle accompanied by a decrease of ripple amplitudes is observed. This contradiction to present models of pattern formation, either of redistributive or stress-induced solid flow origin, might be solved by introducing an additional non-local process to the existing models as pointed out by Davidovitch *et al* [63] Originally, a non-local damping term for pattern formation was proposed by Facsko *et al* [64], which mimics the preferred re-deposition of sputtered material into valleys compared to hillocks. Simulations for the re-deposition mechanism in a first simple approximation predict a transition from instability to stability/smoothing under large damping conditions [64]. A similar effect, namely the preferred erosion of adjacent protrusions, can be caused by reflected ions. At this point it can only be speculated if a surface stabilization or smoothing can arise from a large portion of reflected particles. An analogous situation is assumed to be responsible for surface polishing under glancing incidence conditions where most of the ions incident on a nearly perfect plane surface will be specularly reflected after collisions with surface atoms. However, if the ion impinges surface irregularities (e.g. polishing scratches or bumps), where the probability of sputtering off atoms from the surface is significantly higher [65], a smoothing effect is observed. For somewhat smaller ion incidence angles, most ions are still reflected in the forward direction and result in a distinct forward sputtering of initial topographic defects, especially at the upstream side of concave surface regions (depressions). The defect size grows in the direction of ion beam, probably accompanied by a guiding of ions along the defects, similar to the formation of perpendicular mode ripples on metallic surfaces at 83° via a network of coalesced elongated vacancy islands [66, 67].

In this case the initial structure wavelength is set by mean defect separation while ripple coarsening can be again explained as a result of the ion reflection in ion beam direction along the sidewalls according to the Hauffe mechanism. This would coincide with the results for ion erosion of polycrystalline metal films at grazing incidence where the initial surface morphology affects the formation of nanostructures and drives the formation of ripples with a mean wavelength given by the original grain size [68]. Such a kind of pattern can be also interpreted as perpendicular mode ripple pattern, however, induced by ion reflection and sputtering under grazing incidence conditions, alternative to the change of ripple orientation within the BH model.

At this point, it becomes clear that more investigations are necessary for the full explanation of the influence of reflected ions on the surface evolution at large incidence angles. From an experimental point of view this is currently addressed with further investigations for different materials, especially for Si as direct counterpart for the Ge study, presented here, and two oxidic materials, i.e. SiO_2 and Al_2O_3.

5. Summary

In conclusion, surface evolution of Ge by low-energy ion beam erosion with different noble gas ions (Ne, Ar, Kr and Xe) was examined for a wide range of experimental parameters. The dependence on ion incidence angle (0–85°) and ion energy (400–2000 eV) for ion fluences from

1.1×10^{17} up to 1.3×10^{19} cm^{-2} were investigated. In detail it is found that no pattern formation occurs in the case of Ne and Ar ions and ripple formation with Kr and Xe starts at larger incidence angles (approx. 65°). Until this angle surface stabilization or smoothing is found. This supports that former results are affected by Fe co-deposition, allowing the formation of highly regular pattern at small ion incidence angles similar to Si. In the absence of co-deposition only a small angular range for patter formation exists. The incidence angle for the onset of ripple formation depends on ion mass and ion beam energy. With decreasing ion energy, the angle shifts to lower values. The time evolution at specific ion incidence angle reveals a coarsening and faceting of the pattern starting with the earliest erosion times or ion fluence accessible within the experiments. Both observations indicate that gradient-dependent sputtering and reflection of primary ions play crucial role for Ge surface evolution. The results are discussed in detail with respect to recently proposed redistributive or stress-induced models for pattern formation. Based on experimental findings and supported by TRIM.SP simulations, it is speculated that a large angular variation of the sputter yield seems to be a potential requirement for surface instabilities during ion erosion of Ge. Finally, it was assumed that reflected primary ions could contribute to surface stabilization and surface smoothing. This could give rise to a non-local contribution to surface evolution which could also explain the non-diverging ripple wavelength at the ion -incidence angle-dependent stability–instability transition observed in the experiments for Ge.

Acknowledgments

We thank Dr Darina Manova for a critical reading of the manuscript. The authors are grateful to the Deutsche Forschungsgemeinschaft for financial supports through research unit FOR 845.

References

[1] Behner H and Wedler G 1985 Ion-bombardment-induced regularly oriented steps on Fe(110) *Surf. Sci.* **160** 271–9
[2] Carter G, Nobes M J and Whitton J L 1985 Sputtering induced topography development on fcc metals *Appl. Phys.* A **38** 77–95
[3] Rusponi S, Boragno C and Valbusa U 1997 Ripple structure on Ag(110) surface induced by ion sputtering *Phys. Rev. Lett.* **78** 2795–8
[4] Murty M, Curcic T, Judy A, Cooper B, Woll A, Brock J, Kycia S and Headrick R 1998 X-ray scattering study of the surface morphology of Au(111) during Ar^+ ion irradiation *Phys. Rev. Lett.* **80** 4713–6
[5] van Dijken S, de Bruin D and Poelsema B 2001 Kinetic physical etching for versatile novel design of well ordered self-affine nanogrooves *Phys. Rev. Lett.* **86** 4608–11
[6] Malis O, Brock J, Headrick R, Min-Su Yi and Pomeroy J 2002 Ion-induced pattern formation on Co surfaces: an x-ray scattering and kinetic Monte Carlo study *Phys. Rev.* B **66** 035408
[7] Chan W, Pavenayotin N and Chason E 2004 Kinetics of ion-induced ripple formation on Cu(001) surfaces *Phys. Rev.* B **69** 245413
[8] Carter G, Nobes M J, Paton F, Williams J S and Whitton J L 1977 Ion bombardment induced ripple topography on amorphous solids *Radiat. Eff.* **33** 65–73
[9] MacLaren S W 1992 Surface roughness development during sputtering of GaAs and InP: evidence for the role of surface diffusion in ripple formation and sputter cone development *J. Vac. Sci. Technol.* A **10** 468
[10] Elst K 1993 Influence of oxygen on the formation of ripples on Si *J. Vac. Sci. Technol.* B **11** 1968
[11] Malherbe J B 1994 Sputtering of compound semiconductor surfaces: I. Ion–solid interactions and sputtering yields *Crit. Rev. Solid State Mater. Sci.* **19** 55–127

[12] Vajo J J 1996 Influence of O_2^+ energy, flux and fluence on the formation and growth of sputtering-induced ripple topography on silicon *J. Vac. Sci. Technol.* A **14** 2709
[13] Jiang Z X and Alkemade P F A 1998 The complex formation of ripples during depth profiling of Si with low energy, grazing oxygen beams *Appl. Phys. Lett.* **73** 315
[14] Chason E, Erlebacher J, Aziz M J, Floro J A and Sinclair M B 2001 Dynamics of pattern formation during low-energy ion bombardment of Si(001) *Nucl. Instrum. Methods Phys. Res.* B **178** 55–61
[15] Brown A-D and Erlebacher J 2005 Temperature and fluence effects on the evolution of regular surface morphologies on ion-sputtered Si(111) *Phys. Rev.* B **72** 075350
[16] Mayer T M, Chason E and Howard A J 1994 Roughening instability and ion-induced viscous relaxation of SiO_2 surfaces *J. Appl. Phys.* **76** 1633
[17] Umbach C, Headrick R and Chang K-C 2001 Spontaneous nanoscale corrugation of ion-eroded SiO_2: the role of ion-irradiation-enhanced viscous flow *Phys. Rev. Lett.* **87** 246104
[18] Toma A, Buatier de, Mongeot F, Buzio R, Firpo G, Bhattacharyya S R, Boragno C and Valbusa U 2005 Ion beam erosion of amorphous materials: evolution of surface morphology *Nucl. Instrum. Methods Phys. Res.* B **230** 551–4
[19] Tona M, Fujita Y, Yamada C and Ohtani S 2008 Electronic interaction of individual slow highly charged ions with TiO_2(110) *Phys. Rev.* B **77** 155427
[20] El-Said A *et al* 2008 Creation of nanohillocks on CaF_2 surfaces by single slow highly charged ions *Phys. Rev. Lett.* **100** 237601
[21] Gago R, Vázquez L, Cuerno R, Varela M, Ballesteros C and Albella J M 2002 Nanopatterning of silicon surfaces by low-energy ion-beam sputtering: dependence on the angle of ion incidence *Nanotechnology* **13** 304–8
[22] Zhang K, Rotter F, Uhrmacher M, Ronning C, Hofsäss H and Krauser J 2007 Pattern formation of Si surfaces by low-energy sputter erosion *Surf. Coat. Technol.* **201** 8299–302
[23] Madi C S, Bola George H and Aziz M J 2009 Linear stability and instability patterns in ion-sputtered silicon *J. Phys: Condens. Matter* **21** 224010
[24] Keller A and Facsko S 2010 Ion-induced nanoscale ripple patterns on Si surfaces: theory and experiment *Materials* **3** 4811–41
[25] Macko S, Frost F, Ziberi B, Förster D F and Michely T 2010 Is keV ion-induced pattern formation on Si(001) caused by metal impurities? *Nanotechnology* **21** 085301
[26] Ozaydin G, Özcan A S, Wang Y, Ludwig K F, Zhou H, Headrick R L and Peter Siddons D 2005 Real-time x-ray studies of mo-seeded Si) nanodot formation during ion bombardment *Appl. Phys. Lett.* **87** 163104
[27] Sánchez-García J A, Vázquez L, Gago R, Redondo-Cubero A, Albella J M and Czigány Z 2008 Tuning the surface morphology in self-organized ion beam nanopatterning of Si(001) via metal incorporation: from holes to dots *Nanotechnology* **19** 355306
[28] Ozaydin-Ince G and Ludwig K F Jr 2009 *In situ* x-ray studies of native and Mo-seeded surface nanostructuring during ion bombardment of Si(100) *J. Phys.: Condens: Matter* **21** 224008
[29] Sánchez-García J A, Gago R, Caillard R, Redondo-Cubero A, Martin-Gago J A, Palomares F J, Fernández M and Vázquez L 2009 Production of nanohole/nanodot patterns on Si(001) by ion beam sputtering with simultaneous metal incorporation *J. Phys: Condens. Matter* **21** 224009
[30] Zhou J and Lu M 2010 Mechanism of Fe impurity motivated ion-nanopatterning of Si(100) surfaces *Phys. Rev.* B **82** 125404
[31] Cornejo M, Ziberi B, Meinecke C, Hirsch D, Gerlach J W, Höche T, Frost F and Rauschenbach B 2011 Self-organized patterning on Si(001) by ion sputtering with simultaneous metal incorporation *Appl. Phys.* A **102** 593–9
[32] Zhang K, Brötzmann M and Hofsäss H 2011 Surfactant-driven self-organized surface patterns by ion beam erosion *New J. Phys.* **13** 013033
[33] Mark Bradley R 1988 Theory of ripple topography induced by ion bombardment *J. Vac. Sci. Technol.* A **6** 2390

[34] Carter G and Vishnyakov V 1996 Roughening and ripple instabilities on ion-bombarded Si *Phys. Rev.* B **54** 17647–53
[35] Madi C, Anzenberg E, Ludwig K and Aziz M 2011 Mass redistribution causes the structural richness of ion-irradiated surfaces *Phys. Rev. Lett.* **106** 066101
[36] Moseler M 2005 The ultrasmoothness of diamond-like carbon surfaces *Science* **309** 1545–8
[37] Norris S A, Brenner M P and Aziz M J 2009 From crater functions to partial differential equations: a new approach to ion bombardment induced nonequilibrium pattern formation *J. Phys.: Condens: Matter* **21** 224017
[38] Norris S A, Samela J, Bukonte L, Backman M, Djurabekova F, Nordlund K, Madi C S, Brenner M P and Aziz M J 2011 Molecular dynamics of single-particle impacts predicts phase diagrams for large scale pattern formation *Nature Commun.* **2** 276
[39] Castro M and Cuerno R 2012 Hydrodynamic approach to surface pattern formation by ion beams *Appl. Surf. Sci.* **258** 4171–8
[40] Castro M, Gago R, Vázquez L, Muñoz-García J and Cuerno R 2012 Stress-induced solid flow drives surface nanopatterning of silicon by ion-beam irradiation *Phys. Rev.* B **86** 214107
[41] Norris S A 2012 Stress-induced patterns in ion-irradiated silicon: model based on anisotropic plastic flow *Phys. Rev.* B **86** 235405
[42] Chason E, Mayer T, Kellerman B, McIlroy D and Howard A 1994 Roughening instability and evolution of the Ge(001) surface during ion sputtering *Phys. Rev. Lett.* **72** 3040–3
[43] Kim J, Cahill D and Averback R 2003 Surface morphology of Ge(111) during etching by keV ions *Phys. Rev.* B **67** 045404
[44] Carbone D, Alija A, Plantevin O, Gago R, Facsko S and Metzger T H 2008 Early stage of ripple formation on Ge(001) surfaces under near-normal ion beam sputtering *Nanotechnology* **19** 035304
[45] Ziberi B, Cornejo M, Frost F and Rauschenbach B 2009 Highly ordered nanopatterns on Ge and Si surfaces by ion beam sputtering *J. Phys: Condens. Matter* **21** 224003
[46] Anzenberg E, Perkinson J C, Madi C S, Aziz M J and Ludwig K F 2012 Nanoscale surface pattern formation kinetics on germanium irradiated by Kr^+ ions *Phys. Rev.* B **86** 245412
[47] Perkinson J C, Madi C S and Aziz M J 2013 Nanoscale topographic pattern formation on Kr^+-bombarded germanium surfaces *J. Vac. Sci. Technol.* A **31** 021405
[48] Biersack J P and Eckstein W 1984 Sputtering studies with the Monte Carlo program TRIM.SP *Appl. Phys.* A **34** 73–94
[49] Madi C S and Aziz M J 2012 Multiple scattering causes the low energy-low angle constant wavelength topographical instability of argon ion bombarded silicon surfaces *Appl. Surf. Sci.* **258** 4112–5
[50] Ziberi B, Frost F and Rauschenbach B 2006 Pattern transitions on Ge surfaces during low-energy ion beam erosion *Appl. Phys. Lett.* **88** 173115
[51] Bolse W 1994 Ion-beam induced atomic transport through bi-layer interfaces of low- and medium-z metals and their nitrides *Mater. Sci. Eng.* R **12** 7–121
[52] Ziegler J F, Ziegler M D and Biersack J P 2010 SRIM — the stopping and range of ions in matter (2010) *Nucl. Instrum. Methods Phys. Res.* B **268** 1818–23
[53] Bobes O, Zhang K and Hofsäss H 2012 Ion beam induced surface patterns due to mass redistribution and curvature-dependent sputtering *Phys. Rev.* B **86** 235414
[54] Wittmaack K 2004 Reliability of a popular simulation code for predicting sputtering yields of solids and ranges of low-energy ions *J. Appl. Phys.* **96** 2632
[55] Eckstein W 2002 Calculated sputtering, reflection and range values *MPI für Plasmaphysik/Oberflächenphysik Report* IPP 9/132
[56] Moseler M, Rattunde O, Nordiek J and Haberland H 2000 On the origin of surface smoothing by energetic cluster impact: molecular dynamics simulation and mesoscopic modeling *Nucl. Instrum. Methods Phys. Res.* B **164–165** 522–36
[57] Lorbeer J, Teichmann M, Frost F and Rauschenbach B 2014 in preparation

[58] Madi C, Davidovitch B, George H, Norris S, Brenner M and Aziz M 2008 Multiple bifurcation types and the linear dynamics of ion sputtered surfaces *Phys. Rev. Lett.* **101** 246102
[59] Hauffe W 1976 Faceting mechanism in the sputtering process *Phys. Status Solidi* A **35** K93–6
[60] Völlner J, Ziberi B, Frost F and Rauschenbach B 2011 Topography evolution mechanism on fused silica during low-energy ion beam sputtering *J. Appl. Phys.* **109** 043501
[61] Hossain M Z, Freund J B and Johnson H T 2012 Ion impact energy distribution and sputtering of Si and Ge *J. Appl. Phys.* **111** 103513
[62] Sigmund P 1969 Theory of sputtering: I. Sputtering yield of amorphous and polycrystalline targets *Phys. Rev.* **184** 383–416
[63] Davidovitch B, Aziz M and Brenner M 2007 On the stabilization of ion sputtered surfaces *Phys. Rev.* B **76** 205420
[64] Facsko S, Bobek T, Stahl A, Kurz H and Dekorsy T 2004 Dissipative continuum model for self-organized pattern formation during ion-beam erosion *Phys. Rev.* B **69** 153412
[65] Hansen H, Polop C, Michely T, Friedrich A and Urbassek H 2004 Step edge sputtering yield at grazing incidence ion bombardment *Phys. Rev. Lett.* **92** 246106
[66] Hansen H, Redinger A, Messlinger S, Stoian G, Rosandi Y, Urbassek H, Linke U and Michely T 2006 Mechanisms of pattern formation in grazing-incidence ion bombardment of Pt(111) *Phys. Rev.* B **73** 235414
[67] Hansen H, Redinger A, Messlinger S, Stoian G, Krug J and Michely T 2009 Rapid coarsening of ion beam ripple patterns by defect annihilation *Phys. Rev. Lett.* **102** 146103
[68] Toma A, Setina Batic B, Chiappe D, Boragno C, Valbusa U, Godec M, Jenko M and Buatier de Mongeot F 2008 Patterning polycrystalline thin films by defocused ion beam: the influence of initial morphology on the evolution of self-organized nanostructures *J. Appl. Phys.* **104** 104313